AIP Advances

Obtaining simultaneously high crystallinity and sub-bandgap absorption in femtosecond laser hyperdoped black silicon using ion beam etching

Cite as: AIP Advances **11**, 075014 (2021); https://doi.org/10.1063/5.0044678
Submitted: 29 January 2021 • Accepted: 15 June 2021 • Published Online: 06 July 2021

Simon Paulus, Patrick Mc Kearney, Friedemann Völklein, et al.

ARTICLES YOU MAY BE INTERESTED IN

Simultaneous high crystallinity and sub-bandgap optical absorptance in hyperdoped black silicon using nanosecond laser annealing
Journal of Applied Physics **118**, 225303 (2015); https://doi.org/10.1063/1.4937149

Origins of the enhanced broadband absorption in black silicon
Journal of Applied Physics **129**, 163103 (2021); https://doi.org/10.1063/5.0047153

Demonstration of electronic devices in graphitic carbon nitride crystalline film
AIP Advances **11**, 075204 (2021); https://doi.org/10.1063/5.0055141

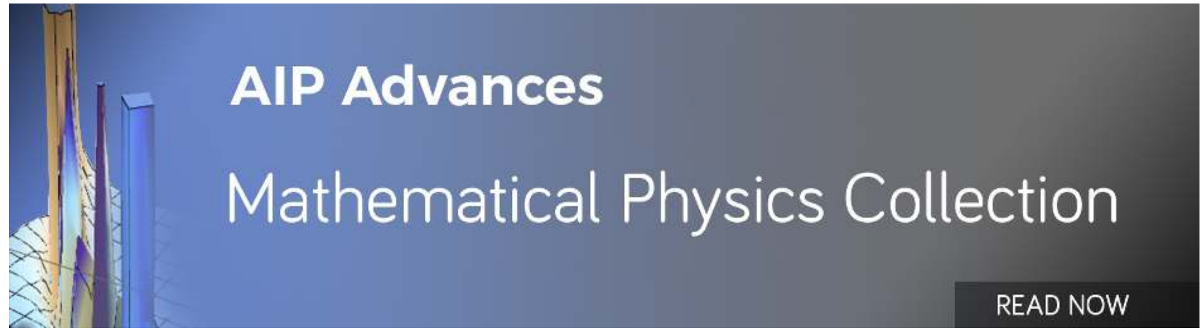

© 2021 Author(s).

Obtaining simultaneously high crystallinity and sub-bandgap absorption in femtosecond laser hyperdoped black silicon using ion beam etching

Cite as: AIP Advances 11, 075014 (2021); doi: 10.1063/5.0044678
Submitted: 29 January 2021 • Accepted: 15 June 2021 •
Published Online: 6 July 2021

View Online

Export Citation

CrossMark

Simon Paulus,[a] Patrick Mc Kearney, Friedemann Völklein, and Stefan Kontermann

AFFILIATIONS

Institute for Microtechnologies (IMtech), University of Applied Sciences RheinMain, Am Brückweg 26, D-65428 Rüsselsheim, Germany

[a]Author to whom correspondence should be addressed: simon.paulus@hs-rm.de

ABSTRACT

Femtosecond laser sulfur hyperdoped silicon (fs-hSi) is capable of absorbing photons in the infrared spectral range while simultaneously exhibiting negligible reflection. However, laser processing creates detrimental amorphous and polycrystalline silicon surface layers impairing electronic properties, especially reducing minority charge carrier lifetimes. This paper demonstrates how to selectively remove these disadvantageous layers by ion beam etching, while crystalline IR-absorbing silicon underneath is left. The increase in silicon crystallinity is quantified by laterally probing the fs-hSi samples with Raman spectroscopy.

© 2021 Author(s). All article content, except where otherwise noted, is licensed under a Creative Commons Attribution (CC BY) license (http://creativecommons.org/licenses/by/4.0/). https://doi.org/10.1063/5.0044678

INTRODUCTION

Texturing of silicon can be achieved by irradiating the surface with ultrashort laser pulses[1] and leads to a low reflective surface morphology. This laser process is even more effective than many conventional antireflection coatings (ARCs).[2,3] The resulting surface morphology strongly depends on laser parameters, such as pulse fluence, laser pulses per spot, and the processing gas atmosphere.[4,5] The resulting structures range in size and morphology from nanometer sized ripples to micrometer sized cones.[6,7] Higher pulse fluence and many pulses per spot lead to a larger and more isotropic surface morphology.[8] Larger surface cones cause more light trapping and exhibit the highest absorptance values.[9]

If the structuring process takes place in a sulfur hexafluoride (SF_6) atmosphere, sulfur is incorporated into the silicon crystal lattice. The SF_6 dissociates through the high laser intensities, and a doping mechanism takes place. The resulting incorporations are sulfur atoms, sulfur ions, and sulfur–sulfur pairs, as well as their ions and other sulfur complexes.[10] These incorporations take up substitutional lattice sites during recrystallization.[10] Sulfur concentrations reaching up to 1 at. % can be achieved.[11,12] These heavily doped layers are of great interest for infrared sensors and photovoltaics because they create energy bands within the bandgap of silicon and hence absorb sub-bandgap light.[13,14] The SF_6 gas pressure, the number of pulses per spot, and the laser fluence are parameters to manipulate the doping profile.[5,15,16] Doping concentrations above 0.6 at. % lead to a metallic electrical behavior of fs-hSi;[17,18] thus, the sulfur doping concentration needs to be kept below this value for good semiconductor device performance. Higher sulfur doping concentrations lead to higher favorable sub-bandgap absorption. However, higher doping concentrations lead to lower charge carrier mobility, which impedes carrier extraction.[17,19] Furthermore, the laser process creates amorphous and polycrystalline surface layers.[4] These highly recombinative layers reduce the effective minority carrier lifetime in fs-hSi and thus impede charge carrier extraction in optoelectronic applications. Considering the mentioned effects, an ideal sulfur concentration and thickness of the doped layer need to be found. In Ref. 17, the ideal sulfur concentration was calculated and measured to a value of $1.4 \cdot 10^{19}$ cm^{-3}; however, this layer got doped by ion implantation and not by femtosecond laser pulses.

© Author(s) 2021

In detail, laser irradiation induces high crystal pressures, which cause crystal defects and the formation of other silicon phases. The laser created crystalline Si–I transforms mainly to amorphous silicon (a-Si) and polycrystalline silicon, such as Si-XII and Si-III.[4,20] To recrystallize the amorphous and polycrystalline layers, thermal annealing is a well-established approach.[21–23] This annealing method successfully restores the crystallinity at the surface.[24] However, the temperature load during annealing also leads to a significant decrease in the sub-bandgap absorption.[25,26] This effect is explained by the fact that the sulfur atoms can diffuse at annealing temperatures and form precipitations on the grain boundaries as well as within the grain. With the so formed sulfur clusters, the sulfur induced energy states in the bandgap of silicon disappear, and thus, the absorption in the sub-bandgap region decreases.[26] By quickly quenching the silicon directly after annealing, the degree of absorption can be partially increased again, but it does not reach the initial value.[25]

Another approach to recrystallize silicon is ns-laser annealing.[27] Nanosecond-laser pulses melt the surface, which resolidifies on a time scale that is orders of magnitude faster compared to thermal annealing. The loss in sub-bandgap absorptance is negligible for ns-annealing because silicon resolidifies faster than the sulfur atoms diffuse and form clusters.[27]

This paper introduces a different approach and restores a crystalline silicon surface by removing the laser induced amorphous and polycrystalline silicon layers with an ion beam etching (IBE) process. The process is adjusted to a thickness of 50–200 nm[4,27] of the detrimental layer. The sulfur concentration profile is given in Ref. 12, and we assume that after removing the top layer, the sulfur concentration is still high enough to form an intermediate band and low enough to prevent the formation of a metal-like band structure.[28] Furthermore, the IBE process allows us to adjust the thickness of the sulfur doped layer.

EXPERIMENTAL

To fabricate femtosecond laser sulfur hyperdoped silicon (fs-hSi), we placed Czochralski grown silicon wafers with crystal orientation $\langle 111 \rangle$ in a vacuum chamber, which is evacuated to a pressure below $1 \cdot 10^{-2}$ mbar. Then, the sulfur hexafluoride (SF_6) pressure is set manually and hence varies from 700 to 800 mbar. A constant gas flow of about 500 SCCM was adjusted. A Spectra-Physics Ti:sapphire femtosecond laser amplification system (800 nm wavelength, 100 fs pulse duration, 2 kHz repetition rate, 275 μJ pulse energy) is used to generate ultrashort laser pulses. Mirrors direct the laser beam into the vacuum chamber, which is mounted on a motorized x–y stage. The laser beam is focused on the silicon surface with a confocal lens (focal length 400 mm). To measure the laser spot diameter, a line of fs-hSi is written on a silicon wafer and is measured with a scanning electron microscope (SEM). Hence, the diameter does not represent the full width half maximum of the laser beam but the effective spot diameter that creates structural changes on the silicon surface.

The samples are processed with 200 and 500 laser pulses per effective spot diameter. For the samples processed with 500 pulses per spot, the spot diameter is set to 166 μm, and for the samples processed with 200 pulses per spot, the spot diameter is set to 147 μm, leading to a peak fluence of 2.54 and 3.24 J/cm^2, respectively. The structured area measures 5×5 mm^2.

After laser structuring, amorphous surface layers are removed by IBE. For IBE processing, the IBE chamber is evacuated to a pressure of $3 \cdot 10^{-6}$ mbar, where a Kaufman ion source delivers an ion beam diameter of about 8 cm. Argon ions are extracted from the discharge plasma of the Kaufman source with an acceleration voltage of 1000 V and neutralized after acceleration by electron emission from a tungsten cathode. For the experiments, the ion beam source operates at 0.55 A discharge current, 100 V discharge voltage, 80 mA ion beam current, 2 mA acceleration current, and 100 mA neutralizer emission current. During the IBE, the vacuum pressure in the chamber increases to $2.4 \cdot 10^{-4}$ mbar.

The ion beam etching time of fs-hSi is varied to realize different etching depths. The achieved etching depth on fs-hSi differs from the etching depth on non-structured silicon due to the angle dependence of the ion induced sputtering and the different material properties. The fs-hSi surface is amorphous, which leads to a different etching rate compared to the crystalline silicon (c-Si) surface. However, it is difficult to measure the etching depth on the fs-hSi area, so the etching rate at the c-Si area is measured instead. To determine the etching rate at the c-Si area, the wafer is coated with a patterned photoresist mask, which can be removed after IBE. The etching depth achieved on c-Si is determined with a tactile profilometer (DEKTAK^3).

The surface morphology is examined with a SEM where the acceleration voltage of the electrons is set to 10 kV and the structure is observed under an angle of 30°.

The optical properties are studied with a UV/Vis/NIR spectrometer from PerkinElmer (Lambda-750) and a matching integration sphere from the same manufacturer. For wavelengths below 810 nm, a photomultiplier tube (PMT) is used, and for wavelengths above 810 nm, an InGaAs-detector is used. The wavelength step size is 10 nm, and the integration time for every step is set to 0.6 s. The observed wavelength spectrum ranges from 250 to 2000 nm. The data of three samples, processed with the same parameters, are averaged.

The crystallinity of the samples is measured with a DXR-Raman-microscope from Fischer Scientific, where a laser with a wavelength of 785 nm and a power of 30 mW is focused to a 1.9 μm spot on the surface. The integration time for each Raman spectrum is 0.5 s, and for each measurement, a variety of spectra are taken with 10 μm distance between the measuring points.

RESULTS

The fs-hSi areas show polycrystalline and amorphous peaks in the Raman spectra directly after the laser processing procedure shown in Fig. 1. The ion beam treatment removes the surface layer successively. The etching depth is 23 nm for every etch step, and after each step, the crystallinity is studied again. In Fig. 1, selected Raman spectra are shown for increasing etching depth as well as a reference spectrum of the non-structured surface (black curve). Every spectrum is normalized so that the c-Si peak at 520 cm^{-1} equals a Raman intensity of 1. It is clearly noticeable that the amorphous peaks denoted with a-Si$_1$ and a-Si$_2$ and the polycrystalline peaks denoted with Si-I–Si-XII decrease with increasing etching depth.

© Author(s) 2021

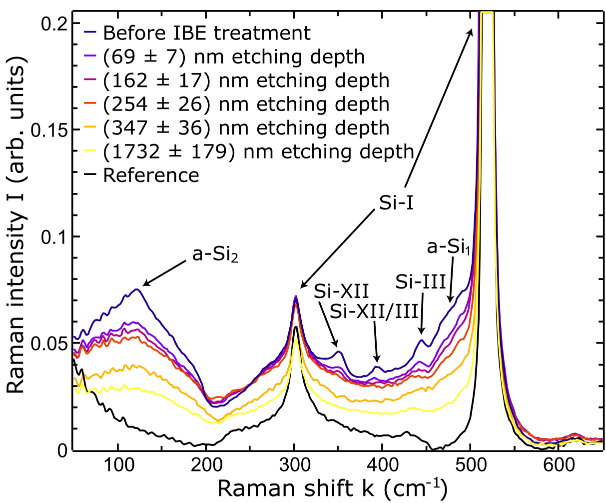

FIG. 1. Raman spectra of fs-hSi samples processed with 200 pulses per spot before IBE treatment and after different etching depths and a reference spectrum of c-Si. For each spectrum, the c-Si peak at 520 cm^{-1} is normalized to a Raman intensity of 1. However, the shown Raman intensity is cut off at 0.2 to better show the amorphous and polycrystalline peaks. The etching depth is measured on a non-structured flat silicon surface. The IBE process increases the crystallinity of the surface but does not restore the crystallinity of the reference sample.

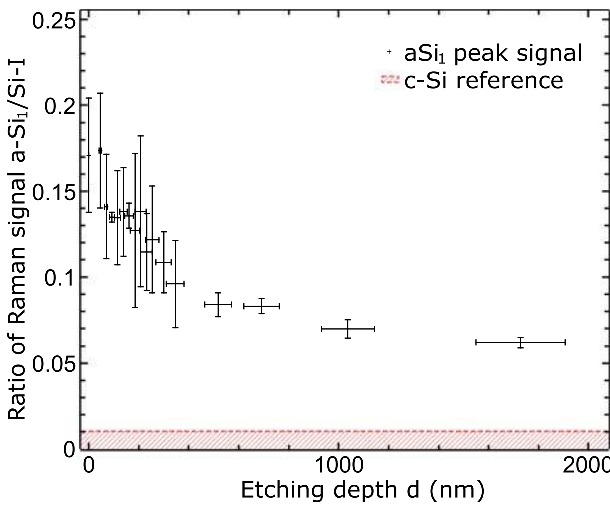

FIG. 2. Ratio of Raman signal of the a-Si_1 peak to the Si–I peak at 520 cm^{-1} as a function of the etching depth. With increasing etching depth, the signal height decreases but does not reach the shown c-Si reference value (red line).

The spectra approach the reference spectrum, but the crystallinity is not restored completely. Furthermore, a slight shift of the peak positions toward lower Raman shifts is observed. This could be due to decreasing compressive stress on the material surface. Less stress leads to decreased Raman shifts.[29] Figure 1 shows the spectra for the samples processed with 200 pulses/spot. The samples processed with 500 pulses/spot show the same behavior.

Even if the reduction of the a-Si_2 peak is more visible, we are focusing on the a-Si_1 peak to compare the results to Ref. 27, where ns-annealing has been studied. Additionally, the a-Si_2 peak is located at low Raman shift values. This could impair a quantitative evaluation of the a-Si_2 peak due to overlaying scattering intensity of the initial laser wavelength. For better comparison, the evaluation of the observed data is performed analogous to Ref. 27. To derive quantitative values for the decreasing amorphous a-Si_1 peak, the range of the a-Si_1 peak is defined from 470 to 490 cm^{-1} in the Raman spectrum. The area under the spectral curve in this range is used to analyze the data. The crystalline Si–I peak from 515 to 525 cm^{-1} is used to normalize the peak area. Figure 2 shows the decrease in the a-Si_1 peak with respect to the etching depth. At an etching depth of 1732 ± 179 nm, the value for the a-Si_1 peak decreased from initially 0.171 ± 0.033 to 0.062 ± 0.003. This equals a relative reduction of 68.0% ± 6.9%.

The surface morphology of a sample processed with 200 pulses/spot directly after fabrication, which was observed with a SEM, is shown in Fig. 3(a). Figure 3(b) shows the surface after an etching depth of 1040 ± 108 nm. At this high etching depth, a smoothening of the surface is clearly visible. The cone-like structure of fs-hSi is still present, but the tips of the cones are beginning to flatten. Again, the samples processed with 500 pulses/spot show similar results.

Figure 4(a) shows the reflectance and transmittance before IBE (dotted line) and after IBE to a depth of (347 ± 36) nm (solid line). This etching depth was chosen because of low amorphous Raman peaks and simultaneously high absorption. The transmittance

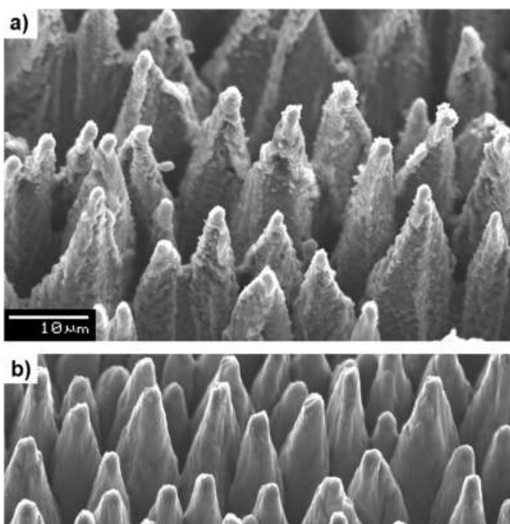
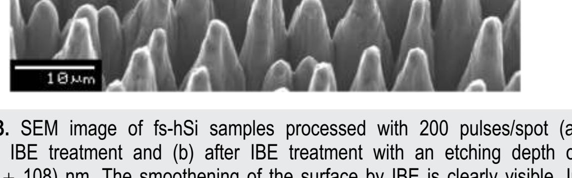

FIG. 3. SEM image of fs-hSi samples processed with 200 pulses/spot (a) before IBE treatment and (b) after IBE treatment with an etching depth of (1040 ± 108) nm. The smoothening of the surface by IBE is clearly visible. In addition, the tips of the cones are flattening.

© Author(s) 2021

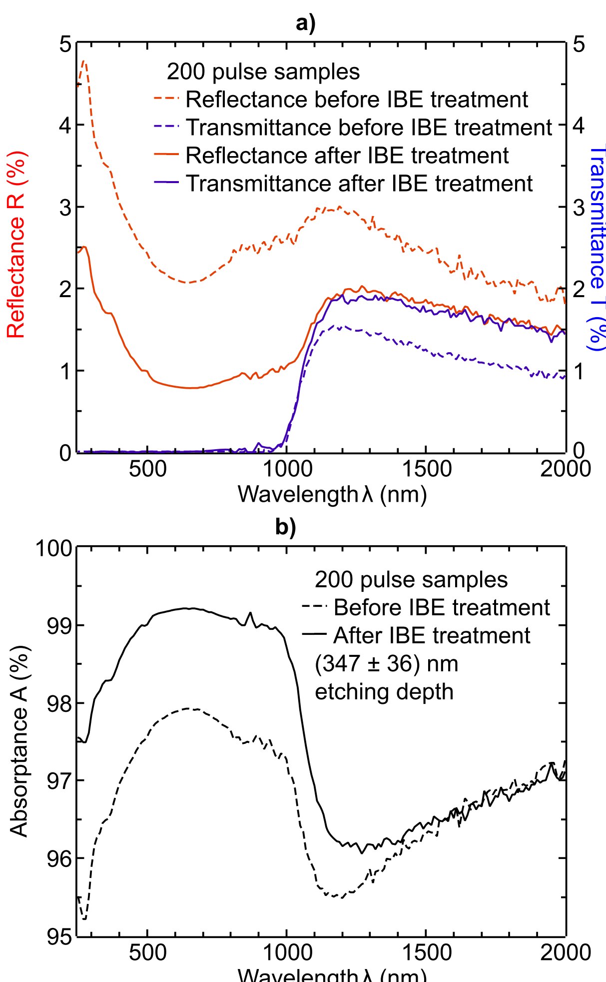

FIG. 4. (a) Reflectance and transmittance before and after IBE treatment at an etching depth of (347 ± 36) nm. A reduction of the reflectance and an increasing transmittance in the IR region are observed. (b) Absorptance before and after IBE treatment.

is increased in the IR region above 1100 nm after the etching procedure. This effect is caused by a decreasing sulfur concentration on the surface and decreasing thickness of the sulfur doped layer due to the removal of the surface. Surprisingly, the reflectance decreases about 2% absolute in the investigated wavelength range. We assume that this is due to the angular dependency of the IBE process leading to a cone shape, which suppresses reflection from the surface more effectively. Figure 4(b) shows that in the spectral range up to 1100 nm, the decreasing reflectance leads to an increase in absorption. Above 1100 nm, the decreasing reflectance and increasing transmittance lead to a nearly unchanged absorption.

It has to be considered that the thermal influence of the IBE process is not negligible. To minimize thermal effects, the etching time should be minimized, and the sample should be cooled while etching. Otherwise, the heat leads to a further decrease in the absorptance in the IR region due to diffusion of the sulfur atoms.[21]

CONCLUSION

This work shows that IBE successfully increases the crystallinity of fs-hSi while conserving the cone-like microstructures and IR absorption properties. Removing the top layers by IBE leads to a decreased sulfur concentration on the surface, which results in an increased transmittance in the wavelength regime above 1100 nm. In order to achieve high crystallinity, the etching depth may exceed the ideal depth, which would lead to a maximized infrared absorption caused by sulfur hyperdoping. In this case, the IBE process can be combined with other post-laser treatments such as ns-annealing to increase crystallinity. Furthermore, the IBE process decreases the reflectance of fs-hSi in the whole investigated wavelength regime, which leads to an enhanced absorption in the visible region. In combination with techniques that lead to a homogeneous doping profile[16] and other annealing techniques such as ns-annealing,[27] IBE is a promising post-laser treatment to achieve high crystallinity and simultaneously control the sulfur concentration in the surface and the thickness of the sulfur doped layer, respectively.

ACKNOWLEDGMENTS

The authors acknowledge financial support from the Deutsche Forschungsgemeinschaft DFG under Grant No. 429413061 and the Federal Ministry of Education and Research of Germany under Grant No. 03INT701AA.

The authors would like to thank Professor Dr. Jutta Kerpen and her team for providing us the opportunity of measuring with the Raman spectrometer and thank Ingo Lebershausen for technical support.

DATA AVAILABILITY

The data that support the findings of this study are available from the corresponding author upon reasonable request.

REFERENCES

[1] T.-H. Her, R. J. Finlay, C. Wu, S. Deliwala, and E. Mazur, Appl. Phys. Lett. **73**, 1673 (1998).

[2] M. Otto, M. Kroll, T. Käsebier, R. Salzer, A. Tünnermann, and R. B. Wehrspohn, Appl. Phys. Lett. **100**, 191603 (2012).

[3] J. M. Warrender, Appl. Phys. Rev. **3**, 031104 (2016).

[4] M. J. Smith, M.-J. Sher, B. Franta, Y.-T. Lin, E. Mazur, and S. Gradečak, J. Appl. Phys. **112**, 083518 (2012).

[5] R. Younkin, J. E. Carey, E. Mazur, J. A. Levinson, and C. M. Friend, J. Appl. Phys. **93**, 2626 (2003).

[6] B. K. Nayak, V. V. Iyengar, and M. C. Gupta, Prog. Photovoltaics **19**, 631 (2011).

[7] A. Y. Vorobyev and C. Guo, Opt. Express **19**(Suppl. 5), A1031–A1036 (2011).

[8] C. H. Crouch, J. E. Carey, J. M. Warrender, M. J. Aziz, E. Mazur, and F. Y. Génin, Appl. Phys. Lett. **84**, 1850 (2004).

[9] C. Wu, C. H. Crouch, L. Zhao, J. E. Carey, R. Younkin, J. A. Levinson, E. Mazur, R. M. Farrell, P. Gothoskar, and A. Karger, Appl. Phys. Lett. **78**, 1850 (2001).

[10] E. Janzén, R. Stedman, G. Grossmann, and H. G. Grimmeiss, Phys. Rev. B **29**, 1907 (1984).

[11] M. A. Sheehy, L. Winston, J. E. Carey, C. M. Friend, and E. Mazur, Chem. Mater. **17**, 3582 (2005).

[12] K.-M. Guenther, T. Gimpel, S. Kontermann, and W. Schade, Appl. Phys. Lett. **102**, 202104 (2013).

© Author(s) 2021

[13]B. Franta, E. Mazur, and S. K. Sundaram, Int. Mater. Rev. **63**, 227 (2018).
[14]K.-M. Guenther, T. Gimpel, J. W. Tomm, S. Winter, A. Ruibys, S. Kontermann, and W. Schade, Appl. Phys. Lett. **104**, 042107 (2014).
[15]M.-J. Sher, N. M. Mangan, M. J. Smith, Y.-T. Lin, S. Marbach, T. M. Schneider, S. Gradečak, M. P. Brenner, and E. Mazur, J. Appl. Phys. **117**, 125301 (2015).
[16]Y.-T. Lin, N. Mangan, S. Marbach, T. M. Schneider, G. Deng, S. Zhou, M. P. Brenner, and E. Mazur, Appl. Phys. Lett. **106**, 062105 (2015).
[17]M.-J. Sher, C. B. Simmons, J. J. Krich, A. J. Akey, M. T. Winkler, D. Recht, T. Buonassisi, M. J. Aziz, and A. M. Lindenberg, Appl. Phys. Lett. **105**, 053905 (2014).
[18]M. T. Winkler, D. Recht, M.-J. Sher, A. J. Said, E. Mazur, and M. J. Aziz, Phys. Rev. Lett. **106**, 178701 (2011).
[19]J. Sickel, A. Ahrens, A. L. Baumann, W. Schade, S. Kontermann, and M. Seibt, Phys. Status Solidi A **214**, 1700264 (2017).
[20]M. J. Smith, Y.-T. Lin, M.-J. Sher, M. T. Winkler, E. Mazur, and S. Gradečak, J. Appl. Phys. **110**, 053524 (2011).
[21]C. B. Simmons, A. J. Akey, J. J. Krich, J. T. Sullivan, D. Recht, M. J. Aziz, and T. Buonassisi, J. Appl. Phys. **114**, 243514 (2013).
[22]T. Gimpel, S. Winter, M. Boßmeyer, and W. Schade, Sol. Energy Mater. Sol. Cells **180**, 168 (2018).
[23]T. Gimpel, K.-M. Guenther, S. Kontermann, and W. Schade, Appl. Phys. Lett. **105**, 053504 (2014).
[24]T. Gimpel, I. Höger, F. Falk, W. Schade, and S. Kontermann, Appl. Phys. Lett. **101**, 111911 (2012).
[25]B. K. Newman, M.-J. Sher, E. Mazur, and T. Buonassisi, Appl. Phys. Lett. **98**, 251905 (2011).
[26]B. R. Tull, M. T. Winkler, and E. Mazur, Appl. Phys. A **96**, 327 (2009).
[27]B. Franta, D. Pastor, H. H. Gandhi, P. H. Rekemeyer, S. Gradečak, M. J. Aziz, and E. Mazur, J. Appl. Phys. **118**, 225303 (2015).
[28]P. Saring, A. Lena Baumann, B. Schlieper-Ludewig, S. Kontermann, W. Schade, and M. Seibt, Appl. Phys. Lett. **103**, 061904 (2013).
[29]G. Sarau, A. Bochmann, R. Lewandowska, and S. Christiansen, *Advanced Aspects of Spectroscopy* (Intech, 2012), p. 221; available at https://www.intechopen.com/books/advanced-aspects-of-spectroscopy/from-micro-to-macro-raman-spectroscopy-solar-silicon-for-a-case-study

© Author(s) 2021